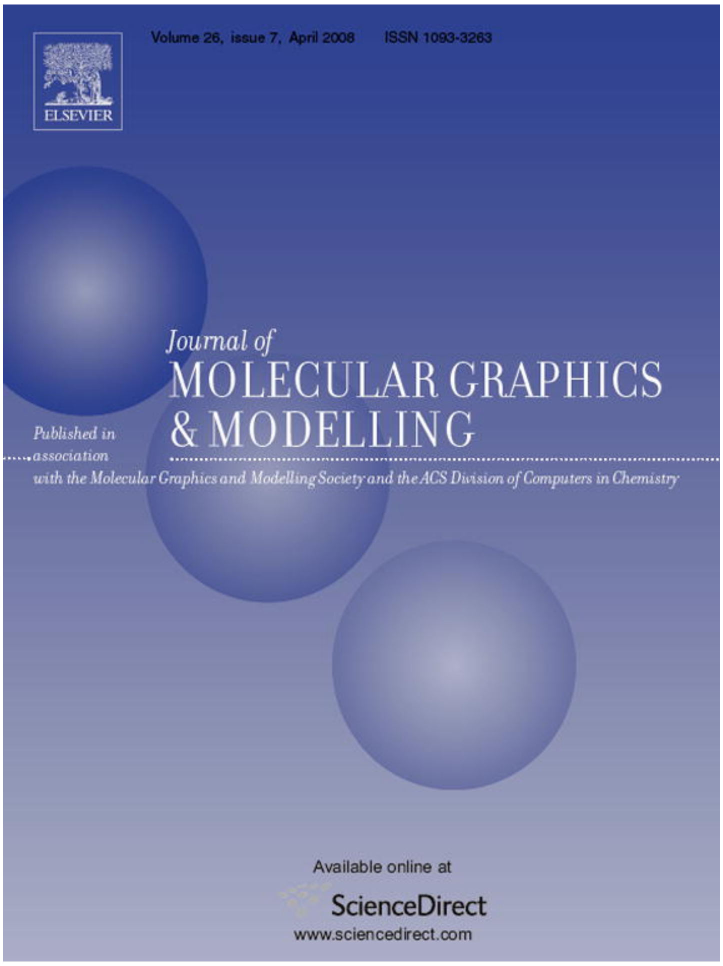
Volume 26, issue 7, April 2008
ISSN 1093-3263
ELSEVIER
Journal of
MOLECULAR GRAPHICS
& MODELLING
Published in association with the Molecular Graphics and Modelling Society and the ACS Division of Computers in Chemistry
Available online at
ScienceDirect
www.sciencedirect.com

Available online at www.sciencedirect.com
ScienceDirect
Journal of Molecular Graphics and Modelling 26 (2008) 1046–1056
Journal of Molecular Graphics and Modelling
www.elsevier.com/locate/JMGM

Visualization of conformational changes of linear short-chain polyethylenes under shear and elongational flows

J.M. Kim, B.J. Edwards *, D.J. Keffer

Department of Chemical and Biomolecular Engineering, University of Tennessee, Knoxville, TN 37996-2200, United States

Received 30 May 2007; received in revised form 28 August 2007; accepted 4 September 2007
Available online 8 September 2007

Abstract

We have performed nonequilibrium molecular dynamic simulations of the linear short-chain polyethylene liquids $C_{24}H_{50}$, $C_{50}H_{102}$, $C_{78}H_{158}$, and $C_{128}H_{258}$ under homogenous shear and elongational flows. We present visualizations of the molecular structure of each of the four liquids under shear and elongation, and compare them with their equilibrium static structures. These graphics provide a structural understanding of the various statistical measures that have been used in the literature to characterize the change in chain conformation as a function of strain rate and chain length. Moreover, these graphics allow a visualization of the inherent chain dynamics and orientation induced by shear and elongational flows. We discuss the molecular-level mechanisms apparent in the graphics.

Keywords: Short-chain polyethylenes; Nonequilibrium molecular dynamics; Entanglement network; Rheological properties; Flow-induced structure

1. Introduction

Fluids with internal microstructure possess thermophysical properties which are functions not only of the local thermodynamic state (e.g., density and temperature), but also of the strength of an applied flow field (i.e., strain rate). One obvious manifestation of this is the fact that polymers are non-Newtonian fluids, meaning that their viscosities are functions of strain rate. Of course, the viscosity is actually a function of state of the internal microstructure, which changes under an imposed strain. Other properties, such as the heat capacity, have also recently been shown to be functions of the polymer microstructure [1,2]. As such, in order to model correctly polymer processes, one must understand the structure/property relationships of polymers under various types of flow.

Molecular-level simulations provide an ideal tool for studying the nonequilibrium structures of polymeric fluids which are difficult to observe experimentally. This is particularly true of polymers undergoing steady, elongational flow at the high elongation rates associated with industrial processing operations. Under these conditions, there currently exists no experimental methodology for measuring the microstructure in this type of flow field. Nonequilibrium molecular dynamics (NEMD) simulations allow one to model fluids undergoing homogeneous shear and elongational flows at arbitrarily high strain rates, in principle.

Much work has been directed at modeling the nonequilibrium structures of flowing polymer melts, and there are many different ways to characterize the flow-induced structural changes in NEMD simulations. One method to characterize changes in flow-induced structure is to use a coarse-grained approach. These approaches are of great interest because they hold the promise of leading to models with fewer degrees of freedom (i.e., a reduction in computational resource requirements), which lend themselves to multiscale modeling efforts. For chain molecules, the most widely used coarse-grained quantity to describe the internal structure of a polymer melt is the conformation tensor, **c**, which is defined as the second moment of the dyadic product of the end-to-end chain vector, $\mathbf{R}_{\text{ete}}$,

$$\mathbf{c} \equiv \langle \mathbf{R}_{\text{ete}} \mathbf{R}_{\text{ete}} \rangle, \tag{1}$$

taken as an ensemble average [3,4]. For the linear, short-chain polyethylenes studied in this work, $C_{24}H_{50}$, $C_{50}H_{102}$, $C_{78}H_{158}$, and $C_{128}H_{25}$, the change in the conformation tensor (or at least the trace of **c**) has been previously reported for steady elongational flow [5–7] and steady shear flow [8].

---

* Corresponding author. Tel.: +1 865 974 9596.
E-mail address: bje@utk.edu (B.J. Edwards).

1093-3263/$ – see front matter © 2007 Elsevier Inc. All rights reserved.
doi:10.1016/j.jmgm.2007.09.001

The conformation tensor, which describes configurational changes in the polymer microstructure, can also be incorporated into continuum evolution equations. In this role, the extra stress tensor is expressed as a function of the conformation tensor via a one-to-one relationship. Then a macroscopic evolution equation for the conformation tensor may be formulated; many such models of polymer viscoelasticity exist [3,4,9,10]. For example, five models representing different categories of constitutive equations were compared to simulation data of *n*-hexadecane under shear and planar elongational flow [8]. By comparing these constitutive equations with NEMD simulations, one can see not only the molecular-level configurational changes quantified by the conformation tensor components, but also changes in the stress tensor that occur in response to the configurational changes in the microstructure.

One can also generate optical properties from NEMD simulations, such as the birefringence tensor. For example, the flow-induced birefringence of model polymer chains has been studied under shear and elongational flows [11,12]. The birefringence is a useful property since it is widely used by experimental rheologists to examine indirectly the internal microstructure of polymer melts. However, birefringence does not necessarily scale linearly with either stress or conformation tensor and, as such, has limitations as a measure of microstructural changes in the fluid [11,12].

Finally, one can represent the structure of a polymer obtained via molecular-level simulation by mapping it onto a coarse-grained entanglement network [7,13–17]. The dynamics of entanglement networks can potentially be modeled [18] and computationally evaluated in a fraction of the time required for a more detailed NEMD simulation. This would allow one to simulate longer polymer chains than is currently feasible strictly via NEMD. For example, in this work, the longest chain we examine is $C_{128}H_{258}$ due to computational limitations, although molecular simulations of longer polyethylene chains have been performed under equilibrium conditions [15,19]. When the chains become fully extended under an elongational flow field, as examined herein, much larger simulation boxes are required to obtain results that are independent of the system size [6].

All of the above measures of polymer configuration, be they molecular-level or coarse-grained, contribute to the overall understanding of the relationship between polymer structure and rheological/thermophysical properties, such as the viscosity and the heat capacity. Each of these measures is also a statistical average over all polymer chains. However, much understanding can be achieved through a direct visualization of the instantaneous configurations of polymeric fluids undergoing shear and elongational flows. In this work, we provide visualizations of $C_{24}H_{50}$, $C_{50}H_{102}$, $C_{78}H_{158}$, and $C_{128}H_{258}$, which span the range from linear alkanes to short-chain, linear polyethylenes, under steady-state and start-up conditions of homogenous shear and elongational flows. These graphics are visual representations of polymer structure as a function of type and strength of flow field and chain length. They are intended to complement the aforementioned statistical measures presented in prior publications [5–8].

2. Simulation methodology

The *NVT* NEMD simulations were performed using the p-SLLOD equations of motion [20] with the Nosé–Hoover thermostat [21]. These equations are

$$\dot{\mathbf{q}}_{ia} = \frac{\mathbf{p}_{ia}}{m_{ia}} + \mathbf{q}_{ia}\cdot\nabla\mathbf{u},\qquad \dot{\mathbf{p}}_{ia} = \mathbf{F}_{ia} - \mathbf{p}_{ia}\cdot\nabla\mathbf{u} - m_{ia}\mathbf{q}_{ia}\cdot\nabla\mathbf{u}\cdot\nabla\mathbf{u} - \zeta\mathbf{p}_{ia}, \tag{2}$$

$$\zeta = \frac{p_\zeta}{Q},\qquad \dot{p}_\zeta = \sum_i\sum_a \frac{p_{ia}^2}{m_{ia}} - DNk_BT,\qquad Q = DNk_BT\tau^2. \tag{3}$$

The $\mathbf{p}_{ia}$ and $\mathbf{q}_{ia}$ represent the momentum and position vectors of atom a of molecule i, respectively. The symbol $\mathbf{F}_{ia}$ denotes the force vector of atom a of molecule i. The m_{ia} is the mass of atom a of molecule i and the $\nabla\mathbf{u}$ is the homogeneous velocity gradient tensor. The Q denotes the inertia mass of the Nosé–Hoover thermostat. The k_B and D represent the Boltzmann constant and the dimensionality of the system, respectively. The symbols ζ and p_ζ quantify the response of the Nosé–Hoover counterparts of the position and momentum variables. The N, V, and T stand for total number of atoms, volume of the system, and absolute temperature, respectively.

Eq. (2) differs from the SLLOD equations [20,21] only in the penultimate term on the right side of the bottom equation. In planar Couette flow (PCF), the only nonzero component of the velocity gradient tensor is $\nabla_y u_x = \dot{\gamma}$, where x is the direction of flow, y is the direction of shear, and $\dot{\gamma}$ is the shear rate. Hence the p-SLLOD equations of motion are the same as the SLLOD equations [20] because the term $m_{ia}\mathbf{q}_{ia}\cdot\nabla\mathbf{u}\cdot\nabla\mathbf{u}$ vanishes. For planar elongational flow (PEF), the nonzero components of the velocity gradient tensor are $\nabla_x u_x = \dot{\varepsilon}$ and $\nabla_y u_y = -\dot{\varepsilon}$, where x is the direction of extension, y the direction of compression, and $\dot{\varepsilon}$ is the elongational strain rate. For a recent discussion of the relative merits of the SLLOD and p-SLLOD algorithms, see Refs. [22–25].

The p-SLLOD equations of motion were integrated with the Nosé–Hoover thermostat using the multiple time scale reversible reference system propagator algorithm (r-RESPA) developed by Tuckerman et al. [26]. The long time scale for the intermolecular interactions was 2.35 fs under PCF and 2.26 fs under PEF. The short time scale for the intramolecular interactions was 0.452 fs under PCF and 0.226 fs under PEF, except for $C_{24}H_{50}$ under PCF, in which case it was 0.235 fs.

The simulations were performed using the Siepmann–Karaboni–Smit (SKS) united-atom model for linear alkanes [27]; however, the rigid bond between adjacent atoms was substituted with a harmonic potential function to simplify the numerical integration without sacrificing the pertinent dynamical behavior. The four types of interactions present in this model are expressed in terms of the Lennard–Jones (LJ) intermolecular and intramolecular potential function,

$$V_{LJ}(r) = 4\varepsilon_{ij}\left[\left(\frac{\sigma_{ij}}{r}\right)^{12} - \left(\frac{\sigma_{ij}}{r}\right)^{6}\right], \tag{4}$$

the bond-stretching harmonic potential,

$$V_{\rm str}(l) = \frac{1}{2}k_{\rm str}(l - l_{\rm eq})^2, \quad (5)$$

the bond-bending harmonic potential,

$$V_{\rm ben}(\theta) = \frac{1}{2}k_{\rm ben}(\theta - \theta_{\rm eq})^2, \quad (6)$$

and the bond-torsional potential [28],

$$V_{\rm tor}(\phi) = \sum_{m=0}^{3} a_m(\cos\phi)^m. \quad (7)$$

In these expressions, $r_c = 2.5\sigma_{\rm CH_2}$, $\varepsilon_{\rm CH_2} = 47$ K, $\varepsilon_{\rm CH_3} = 114$ K, $\sigma_{\rm CH_2} = \sigma_{\rm CH_3} = 3.93$ Å, $l_{\rm eq} = 1.54$ Å, $k_{\rm str}/k_{\rm B} = 452{,}900$ K/Å^2, $\theta_{\rm eq} = 114°$, $k_{\rm ben}/k_{\rm B} = 62{,}500$ K/rad^2, $a_0/k_{\rm B} = 1010$ K, $a_1/k_{\rm B} = 2019$ K, $a_2/k_{\rm B} = 136.4$ K, and $a_3/k_{\rm B} = -3165$ K. The intramolecular LJ energy was preset at a cut-off distance of 2.5σ, and included only atoms that were separated by more than three bonds. The parameters ε_{ij} and σ_{ij} were estimated according to Lorentz–Berthelot mixing rules using the expressions $\varepsilon_{\rm ij} = (\varepsilon_{\rm i}\varepsilon_{\rm j})^{1/2}$, $\sigma_{\rm ij} = (\sigma_{\rm i}\sigma_{\rm j})^{1/2}$.

Under PCF, the Lees–Edwards boundary condition [21] was used to perform the simulations. Under PEF, the Kraynik–Reinelt boundary condition (KRBC) was used [29]. The time period for the KRBC application, $t_{\rm p}$, was determined according to $\varepsilon_{\rm p} = \dot{\varepsilon}\, t_{\rm p}$. The Hencky strain value was thus assigned, $\varepsilon_{\rm p} \approx 0.9624$, and the initial orientation angle of the simulation box was specified as $\theta_0 = 31.718°$.

To analyze the entanglement networks of the simulated liquids, the *Z*-code developed by Kröger [14,16] was applied to the simulation output data. Details concerning the development and algorithm of the *Z*-code can be found in Refs. [14–16].

In general, the simulations were performed at the temperature of 450 K, except for $C_{24}H_{50}$, which was performed at 333 K under both PCF and PEF. The densities of each alkane were $\rho = 0.7728$ g/cm^3 for $C_{24}H_{50}$, $\rho = 0.7426$ g/cm^3 for $C_{50}H_{102}$, $\rho = 0.7640$ g/cm^3 for $C_{78}H_{158}$, and $\rho = 0.7754$ g/cm^3 for $C_{128}H_{258}$, at the temperatures indicated above. For PCF, 100 molecules and 2400 interaction sites were used for $C_{24}H_{50}$, 120 molecules and 6000 interaction sites for $C_{50}H_{102}$, 160 molecules and 12,480 interaction sites for $C_{78}H_{158}$, and 256 molecules and 32,768 interaction sites for $C_{128}H_{258}$. For PEF, 100 molecules and 2400 interaction sites were used for $C_{24}H_{50}$, 96 molecules and 4800 interaction sites for $C_{50}H_{102}$, 192 molecules and 14,976 interaction sites for $C_{78}H_{158}$, and 416 molecules and 53,248 interaction sites for $C_{128}H_{258}$.

The sizes of the simulation boxes had to be specified very carefully in order to avoid system–size effects. The box dimensions for $C_{24}H_{50}$ at equilibrium, and under PCF and PEF, were 41.72 Å × 41.72 Å × 41.72 Å in (x, y, z) space. For PCF, the box dimensions were 93.02 Å × 45.00 Å × 45.00 Å for $C_{50}H_{102}$, 130.50 Å × 54.00 Å × 54.00 Å for $C_{78}H_{158}$, and 212.70 Å × 68.00 Å × 68.00 Å for $C_{128}H_{258}$. For PEF, the box dimensions, were 65.45 Å × 65.45 Å × 35.18 Å for $C_{50}H_{102}$, 100.50 Å × 100.50 Å × 45.20 Å for $C_{78}H_{158}$, and 166.00 Å × 166.00 Å × 58.00 Å for $C_{128}H_{258}$.

Visualizations are presented below for the *NVT* NEMD simulations of these liquids under static equilibrium conditions, under PCF at the dimensionless shear rate, $\dot{\gamma}* \equiv \dot{\gamma}t_{\rm ref}$, of 0.8, and under PEF at the dimensionless elongation rate, $\dot{\varepsilon}* \equiv \dot{\varepsilon}t_{\rm ref}$, of 0.2. The reference time, $t_{\rm ref}$, is defined as $(m\sigma^2/\varepsilon)^{1/2}$, and the strain rates were rendered dimensionless using σ and ε.

3. Results and discussion

Snapshots of $C_{78}H_{158}$ under equilibrium, steady-state shear at a reduced shear rate of 0.8, and steady-state elongational flow at a reduced strain rate of 0.2 are displayed in Fig. 1. These

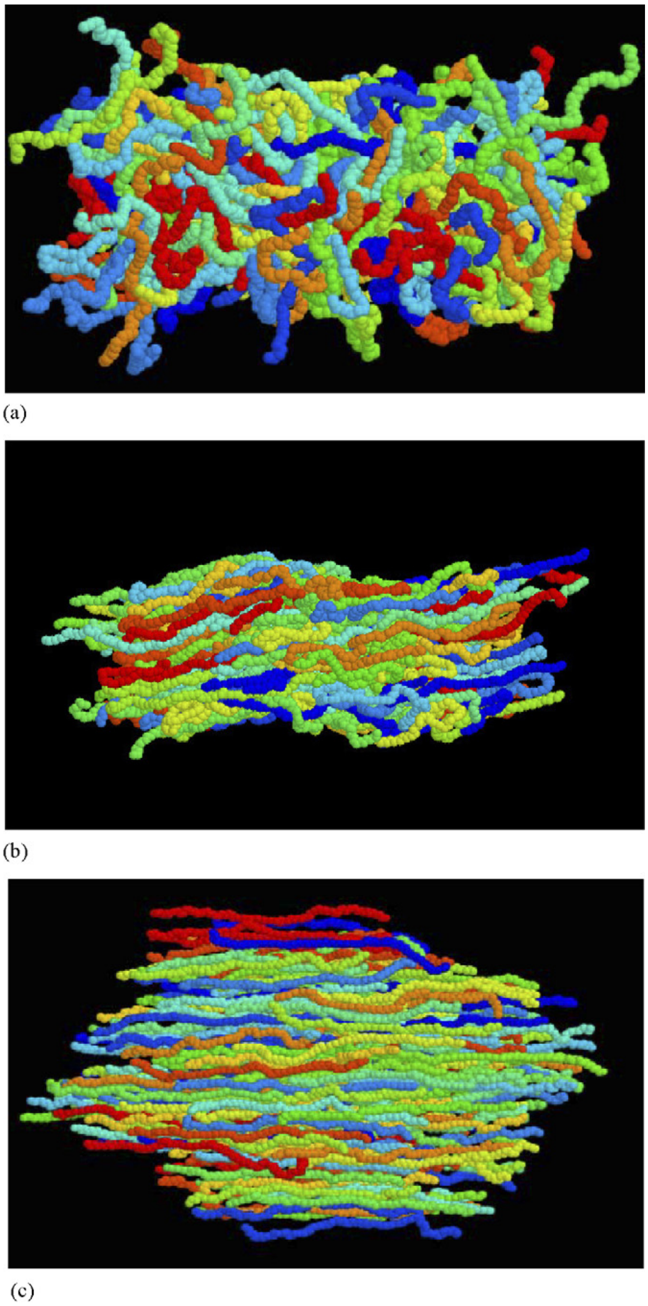
(a)
(b)
(c)

Fig. 1. All chains of $C_{78}H_{158}$ at equilibrium (a), reduced shear rate of 0.8 (b), and elongation rate of 0.2 (c).

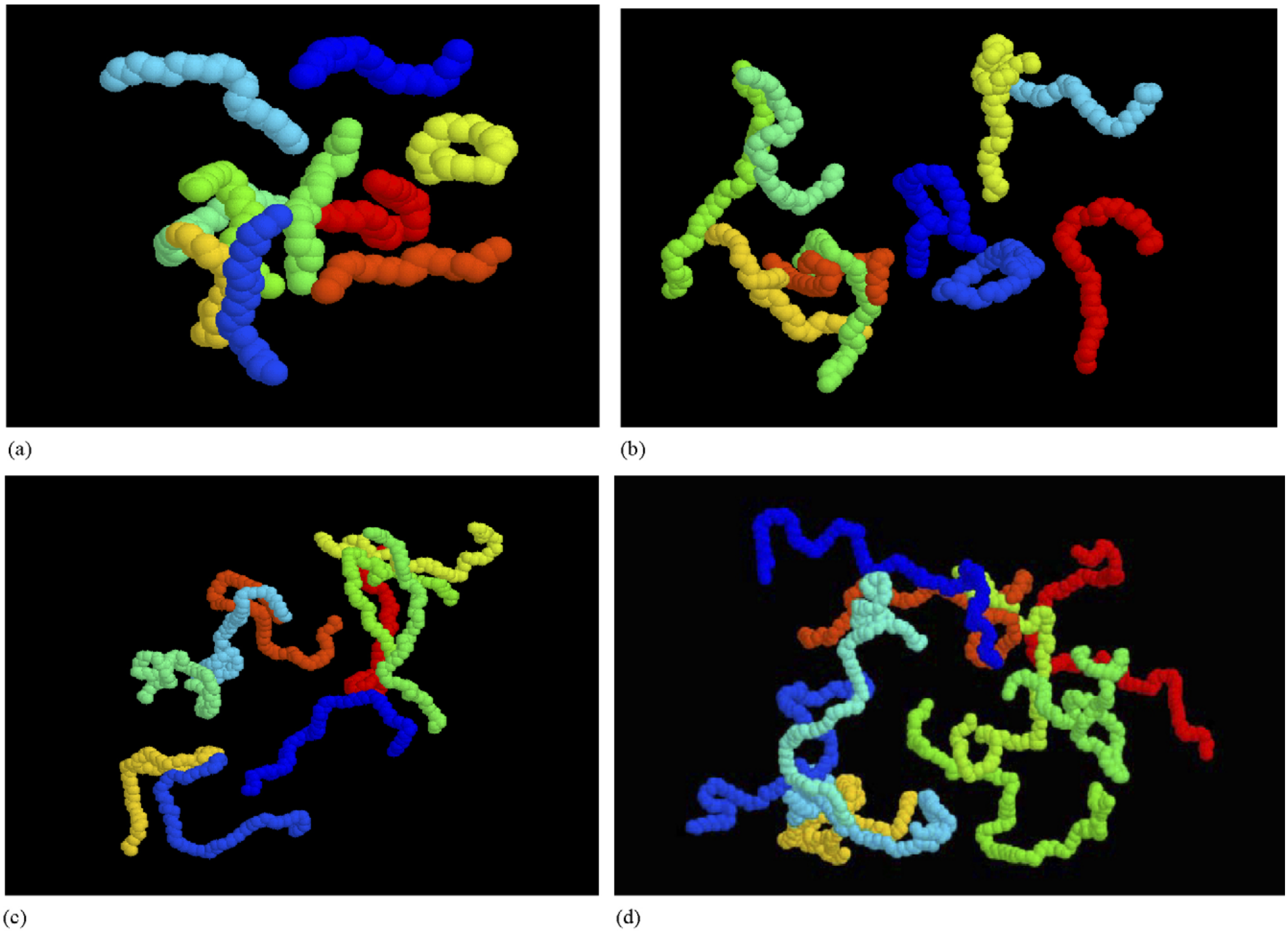

Fig. 2. Ten random chains of $C_{24}H_{50}$ (a), $C_{50}H_{102}$ (b), $C_{78}H_{158}$ (c), and $C_{128}H_{258}$ (d) at equilibrium.

values were so chosen for two reasons. First, they were the maximum values for each flow type which could be safely simulated without observing system size effects or thermostat artifacts. Second, these values correspond to equivalent rates of deformation, as quantified through use of the second invariant of the deformation rate tensor for an incompressible fluid, tr ($\mathbf{D}\cdot\mathbf{D}$) [4]. Here, $\mathbf{D}$ is the symmetric contribution to the velocity gradient tensor, so that tr ($\mathbf{D}\cdot\mathbf{D}$) for elongational flow at a given value of $\dot{\varepsilon}$ is four times larger than tr ($\mathbf{D}\cdot\mathbf{D}$) for shear flow at an equivalent value of $\dot{\gamma}$, i.e., $\mathrm{tr}\,(\mathbf{D}\cdot\mathbf{D}) = \dot{\gamma}/2$ and $2\dot{\varepsilon}$.

In Fig. 1, it is evident that the structure and orientation of $C_{78}H_{158}$ is substantially different under the three conditions. In Figs. 2(c), 3(c), and 4(c), the same snapshots as in Fig. 1 are displayed rendering all but 10 random chains invisible, so that a greater degree of clarity is achieved with respect to the individual molecular structure. In Fig. 2, snapshots of each of the four liquids ($C_{24}H_{50}$, $C_{50}H_{102}$, $C_{78}H_{158}$, and $C_{128}H_{258}$) are displayed at equilibrium. Figs. 3 and 4 display a random 10 chains for the same four fluids under steady-state shear and steady-state elongation, respectively.

The following trends are evident from Fig. 2. Under equilibrium conditions (Fig. 2), the chains are randomly oriented, in terms of an end-to-end vector drawn between the beads on the chain ends. This vector obeys a well-defined Gaussian distribution characterizing its magnitude and direction. The mean-square of the chain end-to-end vector, $\langle \mathbf{R}_{\mathrm{ete}}^2 \rangle$, quantifies the average conformation of the ensemble of chains. For example, the quantity $\langle \mathbf{R}_{\mathrm{ete}}^2 \rangle^{1/2}$ of $C_{128}H_{258}$ under equilibrium conditions is 50.66 Å, whereas the length of the fully stretched chain in the *all-trans*-conformation is 164 Å [7]. As chain length increases, the magnitude of the root mean square end-to-end vector, $\langle \mathbf{R}_{\mathrm{ete}}^2 \rangle^{1/2}$, increases according to the well-known scaling factor of $\sqrt{n}$ [30,31], n being the number of bonds in a single chain (see Table 1); however, the orientation of the chains remains random. Also, although the molecules are relatively uncoiled at low chain lengths, as the molecular weight of the compound increases, the chains increasingly assume random coil conformations. The ratio of $\langle \mathbf{R}_{\mathrm{ete}}^2 \rangle$ with respect to the mean square of the radius of gyration, $\mathbf{R}_{\mathrm{g}}$, decreases toward the theoretical value of six for long polymer chains; however, it will not plateau at this value until $n \approx 140$ [15]. The Kuhn length, $\langle \mathbf{R}_{\mathrm{ete}}^2 \rangle^{1/2}/\sqrt{n}$, which is twice the persistence length, increases from 4.21 Å to 4.50 Å as the chain length increases, indicating a fairly flexible chain.

The orientations and conformations of the chains are determined by entropic considerations alone. Increasing the chain length renders accessible many more possible chain conformations, thus increasing the intrachain entropy. The

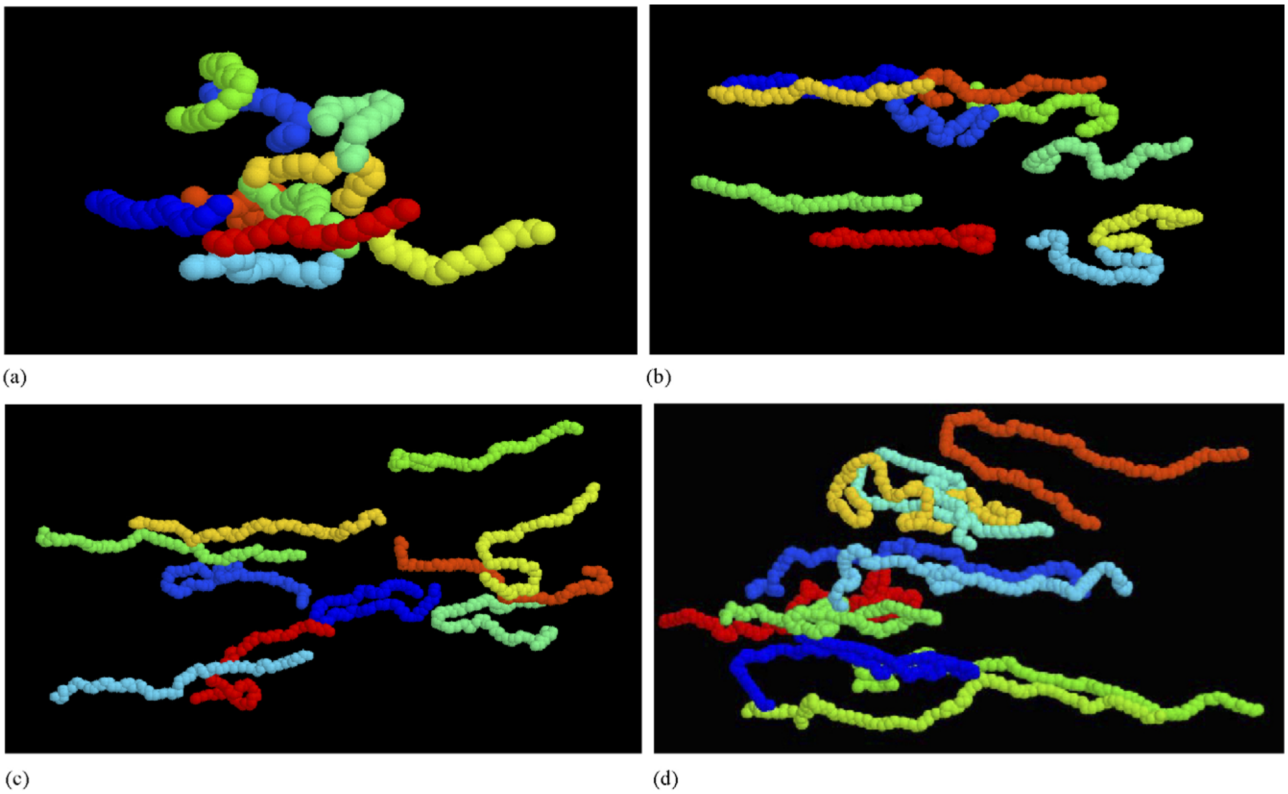
(a) (b) (c) (d)

Fig. 3. Ten random chains of $C_{24}H_{50}$ (a), $C_{50}H_{102}$ (b), $C_{78}H_{158}$ (c), and $C_{128}H_{258}$ (d) at a reduced shear rate of 0.8.

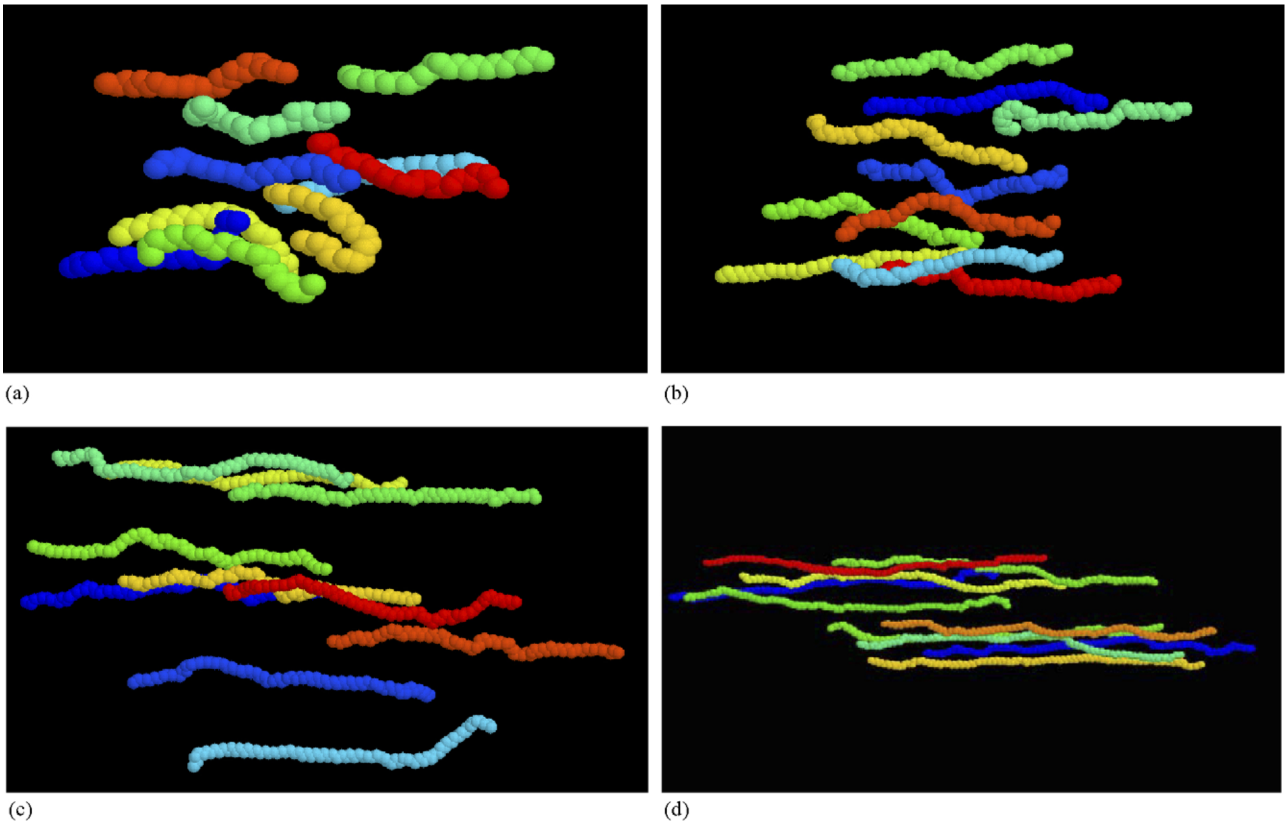
(a) (b) (c) (d)

Fig. 4. Ten random chains of $C_{24}H_{50}$ (a), $C_{50}H_{102}$ (b), $C_{78}H_{158}$ (c), and $C_{128}H_{258}$ (d) at reduced shear rate of 0.2.

Table 1
Statistical measures of polymer configurations for all four liquids at equilibrium, in PCF, and in PEF

Liquid	$\langle \mathbf{R}_{\mathrm{ete}}^2 \rangle^{1/2}$ (Å) equilibrium	$\langle \mathbf{R}_{\mathrm{ete}}^2 \rangle^{1/2}$ (Å) PCF (0.8)	$\langle \mathbf{R}_{\mathrm{ete}}^2 \rangle^{1/2}$ (Å) PEF (0.2)	$\langle \mathbf{R}_{\mathrm{ete}}^2 \rangle^{1/2}$ (Å) full extension	$\langle \mathbf{R}_{\mathrm{ete}}^2 \rangle / \langle \mathbf{R}_{\mathrm{g}}^2 \rangle$ equilibrium	Kuhn length (Å) equilibrium
$C_{24}H_{50}$	20.20	23.13	25.06	29.7	8.44	4.21
$C_{50}H_{102}$	29.72	35.90	52.92	63.3	7.18	4.25
$C_{78}H_{158}$	38.63	52.76	87.19	99.4	6.84	4.40
$C_{128}H_{258}$	50.66	81.91	149.48	164.0	6.60	4.50

Note that all liquids were simulated at 450 K, except for $C_{24}H_{50}$, which was simulated at 333 K.

entropy increases with increasing chain length according to the expression [30,31]

$$S = c - k_{\mathrm{B}} b^2 \langle \mathbf{R}_{\mathrm{ete}}^2 \rangle, \tag{8}$$

where c is an arbitrary constant, $b^2 = 3/(2nl^2)$, and l represents the bond length.

The shortest primitive path of the chains, L_{pp}, is defined as the contour length of the entanglement network structure divided by the number of chains in the system [15]. This network can be visualized as a system of reptation tubes of diameter $a_{\mathrm{pp}} = \langle \mathbf{R}_{\mathrm{ete}}^2 \rangle / L_{\mathrm{pp}}$. The "number of entanglements", Z_{coil}, can be estimated according to

$$Z_{\mathrm{coil}} = \frac{L_{\mathrm{pp}}^2}{\langle \mathbf{R}_{\mathrm{ete}}^2 \rangle} - 1. \tag{9}$$

Values of these topological characteristic indicators are displayed in Table 2 at equilibrium. The least primitive path displays its minimal value (with respect to an applied flow field) for all chain lengths, as does the tube diameter. L_{pp} is generally greater than or equal to the value of $\langle \mathbf{R}_{\mathrm{ete}}^2 \rangle^{1/2}$ for each chain, since the end-to-end vector only quantifies the distance between the chain ends. As the chain length increases, the chains assume more randomly coiled configurations, and consequently the difference between these two quantities magnifies, i.e., L_{pp} grows faster than $\langle \mathbf{R}_{\mathrm{ete}}^2 \rangle^{1/2}$. For the shorter chains, the tube diameter is of the same order as the primitive path length; this is because of the relatively extended chain configurations, which are relatively stiff at low values of n. It seems reasonable that these shorter chain liquids would not form the tortuous, tube network structures of the longer chain liquids, which have greater entropic degrees of freedom for configurational changes. Therefore, the tube diameter decreases relative to the contour length as the chain length increases. However, the shorter chain liquids form tube arrays more readily than the longer chain liquids, since they are relatively more extended than the longer chains and exhibit fewer entanglements. This explains why a_{pp} decreases with diminishing chain length, whereas the density increases. Z_{coil} increases steadily with chain length, as one would intuitively expect, and for long enough chains this increase is approximately linear [15].

Table 2
Topological characteristic quantities at equilibrium for each liquid: contour length, tube diameter, and number of entanglements [7,15]

Liquid	L_{pp} (Å)	a_{pp} (Å)	Z_{coil}
$C_{24}H_{50}$	20.4	16.7	0.04
$C_{50}H_{102}$	30.2	22.5	0.9
$C_{78}H_{158}$	41.1	28.2	1.6
$C_{128}H_{258}$	58.9	35.2	2.5

In Fig. 3, we display snapshots of the 10 random chains for each liquid under steady-state PCF at a reduced shear rate of 0.8. In these figures, flow is in the horizontal direction and the gradient of velocity is in the vertical direction. By comparing Fig. 2 with Fig. 3, it is evident that the presence of a strong shear flow distorts the equilibrium configurations of the chains: there is a preferential orientation (on average) of the chains with respect to the flow field, and the chains are more highly extended. With regard to the chain end-to-end vector orientation, it is well known under shear flow that the average orientation decreases from 45° relative to the direction of flow at low shear rates, to only a few degrees north of the flow direction at high shear rates [4,5,32]. This high shear rate behavior is fully depicted in the snapshots of Fig. 3. The orientation angle is generally a function of the shear rate, and decreases as shear rate increases [11,33,34]. For these high strain rates, the preferred orientation angle is very nearly parallel to the direction of flow. For example the $C_{50}H_{102}$ displays an ensemble average orientation angle of 5° [11].

The configurations of the individual chains have also been altered by the shear flow: the molecules are preferentially stretched in the appropriate direction relative to the direction of flow (see the preceding paragraph). The longer the chain, the greater the degree of extension that manifests. On account of the vorticity of the macroscopic flow field, the molecules tend to rotate in the clockwise direction, which is also evident in the figure as some molecules are caught in mid rotation. Still, the molecules are not on average even nearly fully extended. For example, the value of $\langle \mathbf{R}_{\mathrm{ete}}^2 \rangle^{1/2}$ of $C_{128}H_{258}$ under PCF, 81.91 Å, is larger than the equilibrium value of 50.66 Å, but much smaller than that of the fully *trans*-conformation, 164 Å.

These graphics also provide a visual understanding of polymer shear-thinning behavior under flow. The preferential alignment of the long chains under flow conditions allows greater freedom of motion along the flow direction than is possible in a randomly oriented sample. Thus at low shear rates, the stress scales linearly with the applied strain rate; however, as an increasing number of chains orient preferentially nearly along the flow direction, a relative stress reduction occurs as the chains are able to glide by each other more freely. In previous studies [5–7], it was observed that weakened intramolecular Lennard–Jones interaction energies between chain atoms and

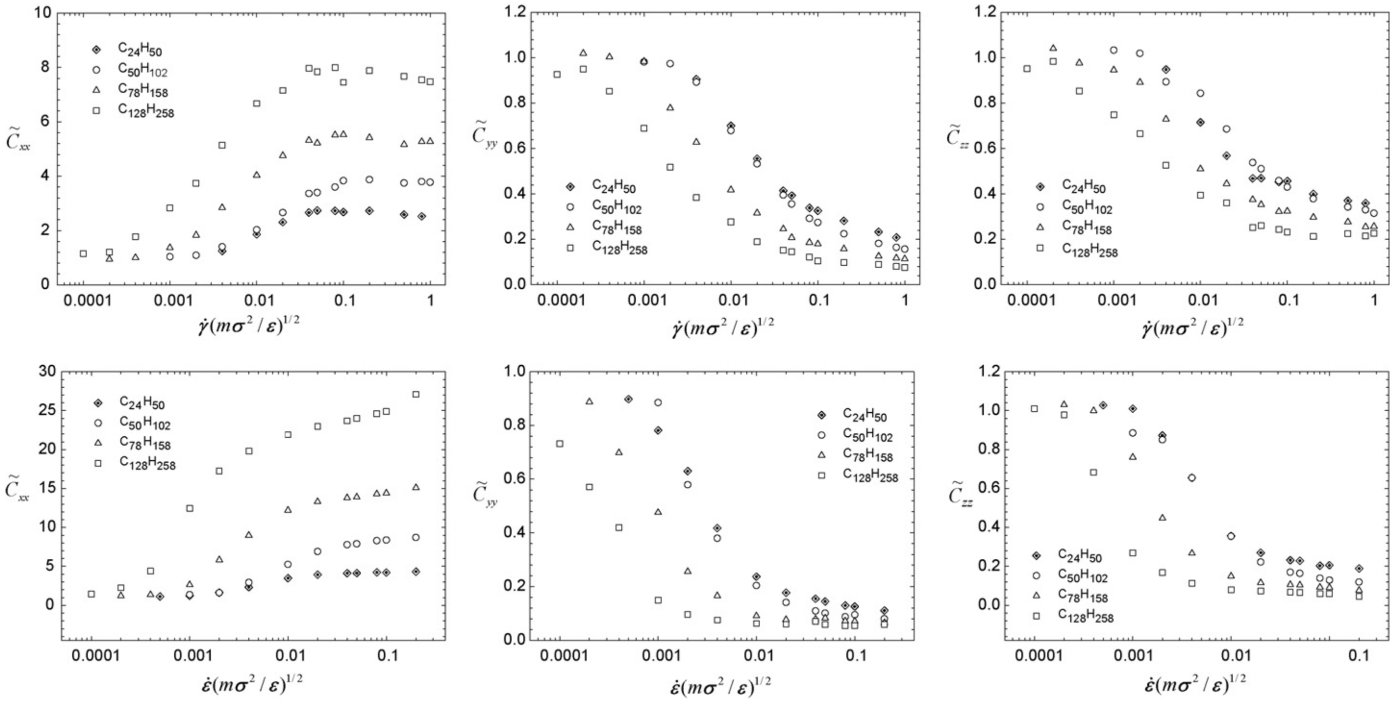

Fig. 5. Conformation tensor components of $C_{24}H_{50}$, $C_{50}H_{102}$, $C_{78}H_{158}$, and $C_{128}H_{258}$ under PCF (upper row) and PEF (bottom row).

stronger intermolecular LJ energies occurred as a result of the chain unfolding (reducing the number of interacting intramolecular pairs) and alignment with other chains (increasing the number of interacting intermolecular pairs).

Ten random chains under an elongational flow of dimensionless strain rate 0.2 are displayed in Fig. 4. The axis of extension lies in the horizontal direction, and the axis of compression lies in the vertical direction. From Fig. 4, it is clear

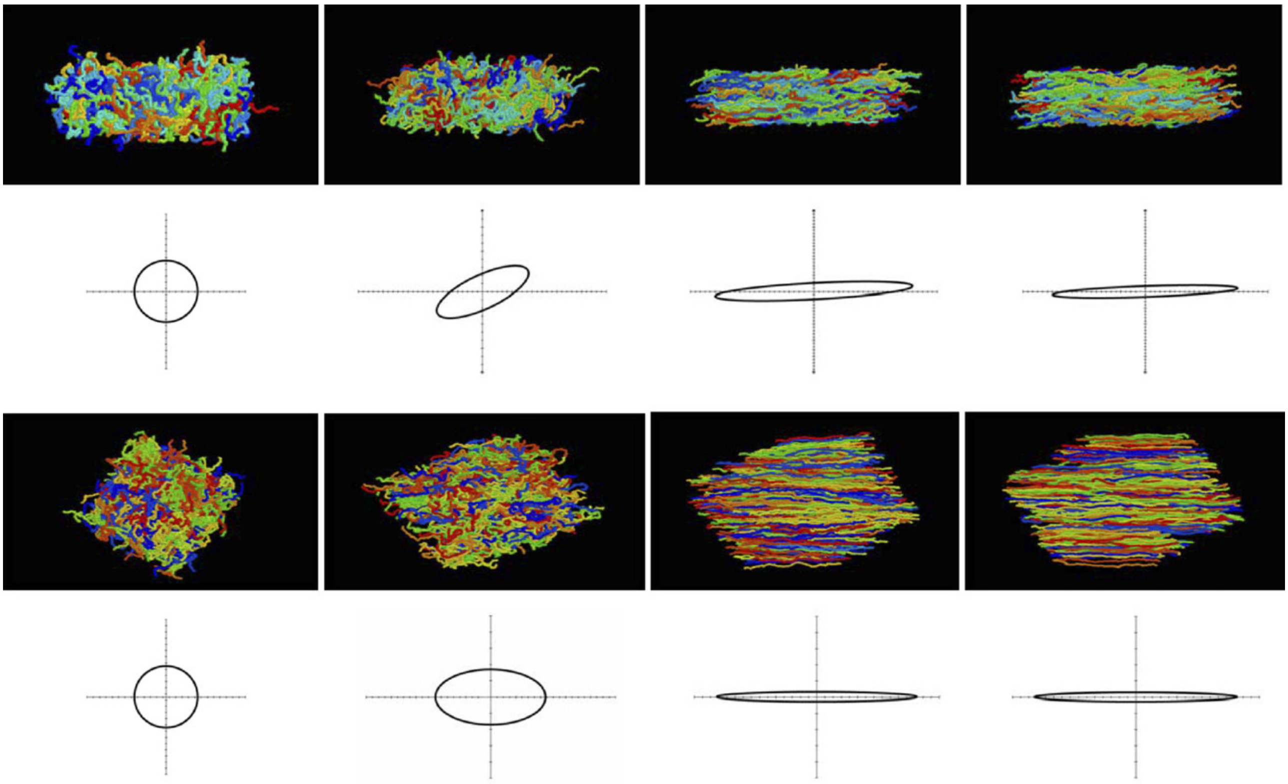

Fig. 6. Snapshots of the molecular structure under PCF (upper row) and PEF (bottom row) and the corresponding distribution functions as determined by the Eigenvalues and Eigenvectors of the conformation tensor. Under PCF, the depictions are for reduced shear rates of 0.0, 0.0004, 0.08, and 0.8, respectively. Under PEF, the snapshots are for reduced elongation rates of 0.0, 0.0004, 0.08, and 0.2, respectively.

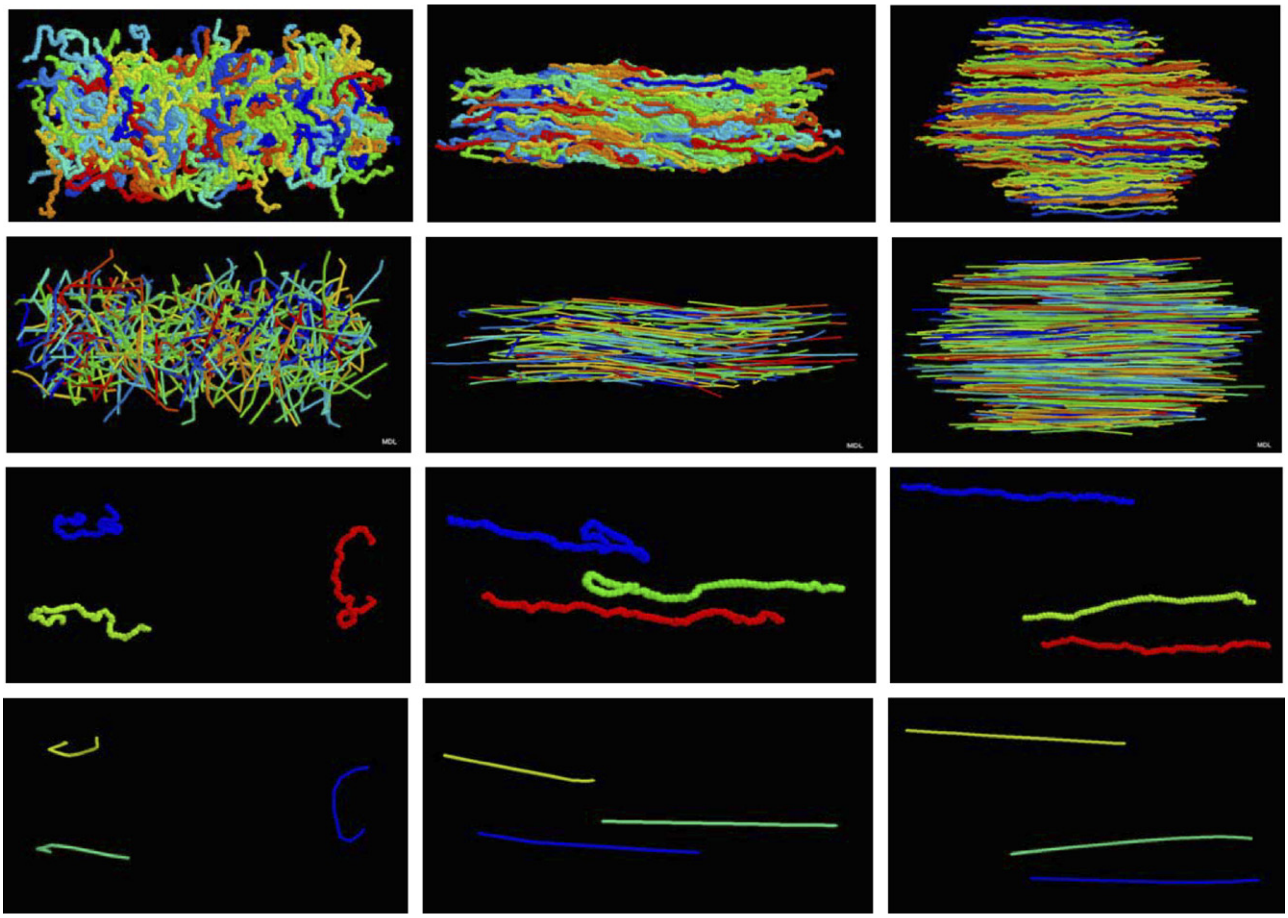

Fig. 7. Projections of atomistic chain structure of $C_{128}H_{258}$ onto shortest primitive path. The first column depicts the equilibrium structure, the second column displays the PCF structure, and the third column presents the PEF structure. The first row shows the corresponding full chain structures to Fig. 1. The second row displays the entanglement networks of the three cases. The third and fourth rows depict the same as above but for only three random chains of the overall liquid system presented in the first two rows.

that the chains of all four liquids align on average with the axis of extension. However, it is also apparent that the relative degree of extension of the chains increases dramatically with chain length. Since elongational flow is vorticity-free, the rotation of the molecules evident in Fig. 3 is not observed. Also, the degree of orientation (i.e., the number of molecules near to the preferred direction) is substantially greater than in the shear flow, and the preferred direction is always in the direction of extension. As the chain length increases, the chains become virtually fully extended: e.g., the value of $\langle \mathbf{R}_{\mathrm{ete}}^2 \rangle^{1/2}$ of $C_{128}H_{258}$ under PEF, 149.48 Å, is larger than that under PCF, 81.91 Å, and approaches that of the fully *trans*-conformation, 164 Å. See Table 1 for a comparison of various statistical quantities for equilibrium and under PCF and PEF for all of the simulated liquids.

Tension-thinning behavior is also observed in these liquids [6]. Fig. 4 provides qualitative information regarding the relative stress reduction on account of chain alignment in the direction of flow. As was the case with shear-thinning behavior, increasing elongation rate leads to an increase in the number of chains aligned with respect to the direction of flow, which in turn results in a decrease of the relative elongational stress. Even though the quantitative change of the intermolecular and intramolecular energies is very different between PCF and PEF, the qualitative change of these energies is very similar, and the same physical explanations apply to the liquids under PEF.

The average extension of the polyethylene chains can be quantified through the conformation tensor of Eq. (1). In Fig. 5, the diagonal components of the dimensionless conformation tensor are plotted under PCF and PEF as functions of strain rate, and the trace is directly related to $\langle \mathbf{R}_{\mathrm{ete}}^2 \rangle$. Here x is the flow direction, y is the gradient or compression direction, and z is the neutral direction. Under quiescent conditions, this tensor is the unit tensor. It is evident from these plots that the chains undergo a dramatic extension in both types of flow at intermediate strain rates, although the degree of extension under PEF is much more severe. Note that in both cases, the molecules extend along the flow direction, and compress along the other two directions increasingly with increasing strain rate. The snapshots of Figs. 3 and 4 were taken at the highest values of the strain rates in Fig. 5.

The distribution of chain conformations and the preferred direction of orientation can be quantified using the Eigenvalues and Eigenvectors of the conformation tensor. In Fig. 6, the circles and ellipsoids represent the distributions of the chain extensions and orientations about the flow direction at various strain rates. For shear flow, the dimensionless shear rates were

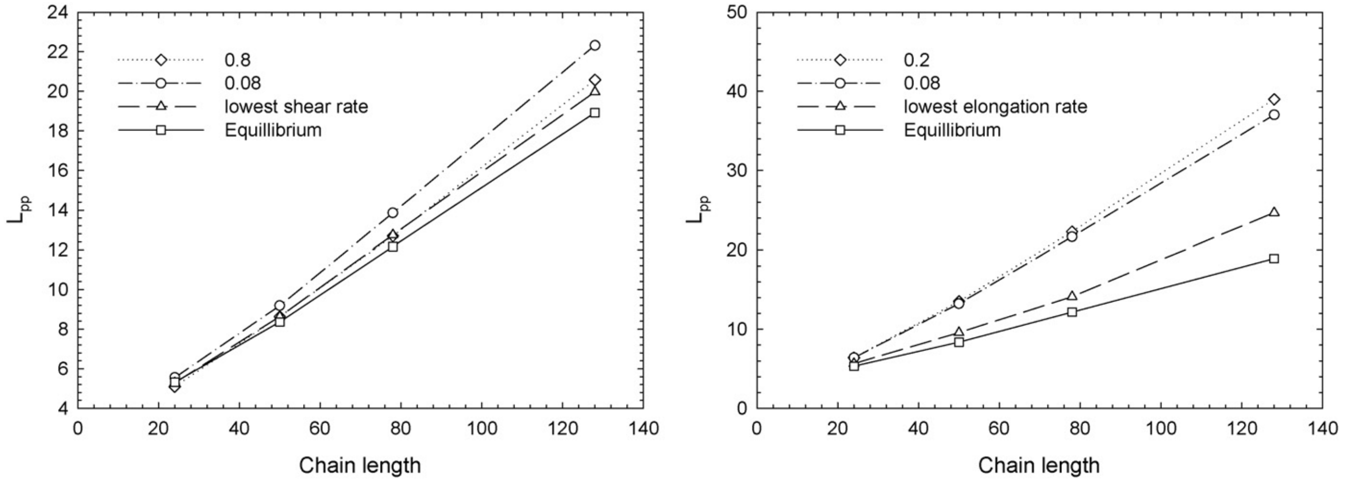

Fig. 8. Dimensionless primitive path length vs. chain length at equilibrium and different values of the applied strain rate under PCF and PEF.

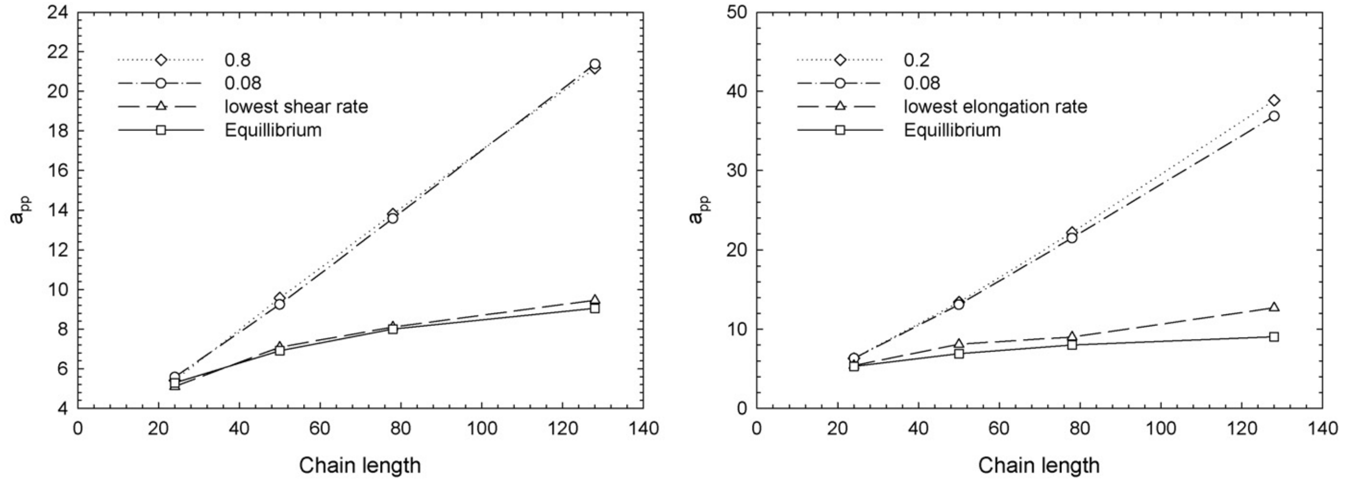

Fig. 9. Dimensionless tube diameter vs. chain length at equilibrium and different values of the applied strain rate under PCF and PEF.

0.0004, 0.08 and 0.8, and for elongational flow the dimensionless elongation rates were 0.0004, 0.08 and 0.2 used. The first column in both rows is the equilibrium state. As expected, at equilibrium all Eigenvalues of the conformation tensor are identical, implying an isotropic distribution of chain end-to-end vectors with a well-defined average magnitude. Under shear flow, the distribution narrows and orients toward the flow direction as the shear rate is increased. Notice that the orientation angle decreases with shear rate relative to the direction of flow. Here, the preferred direction of orientation is quantified by the Eigenvector of the primary Eigenvalue. Under PEF, the distribution becomes much narrower than for shear flow, and always points in the flow direction.

In Fig. 7, we present the entanglement network of the $C_{128}H_{258}$ atomistic chains and the shortest primitive path length at equilibrium (first column), under PCF (second column), and under PEF (third column). The first row is the full atomistic chain system structure, as illustrated in previous figures. The second row presents the full entanglement structure as obtained from the Z-code of Kröger et al. [13–16]. The third row depicts a random three chains for easy visualization, and the bottom row presents the primitive paths for the same three chains. Note the coarse graining of the atomistic chain with many degrees of freedom onto a chain composed of the primitive paths between entanglements bearing much fewer degrees of freedom. At equilibrium, the primitive path length is relatively large as compared to $\langle \mathbf{R}_{\mathrm{ete}}^2 \rangle^{1/2}$, but this difference diminishes as the chains stretch in response to the imposed flow field [7]. This behavior is depicted in Fig. 8.

As the strain rate increases, the degree of extension of the chains under both PCF and PEF increases, thus raising significantly the length of the shortest primitive path. Indeed, under PEF at a very high strain rate, the primitive path is essentially equivalent to the fully extended chain length. Consequently, the number of entanglements decreases as the strain rate increases due to the unraveling of the chains, as might be expected, and the reptation tube diameter grows dramatically [7], as depicted in Fig. 9. Visually, it is also apparent from the snapshots of Fig. 7 that the tube length and diameter increase with increasing strain rate, thus allowing easy conceptualization of the strain-thinning behavior observed in these fluids: as the reptation tube lengthens, the chains are able

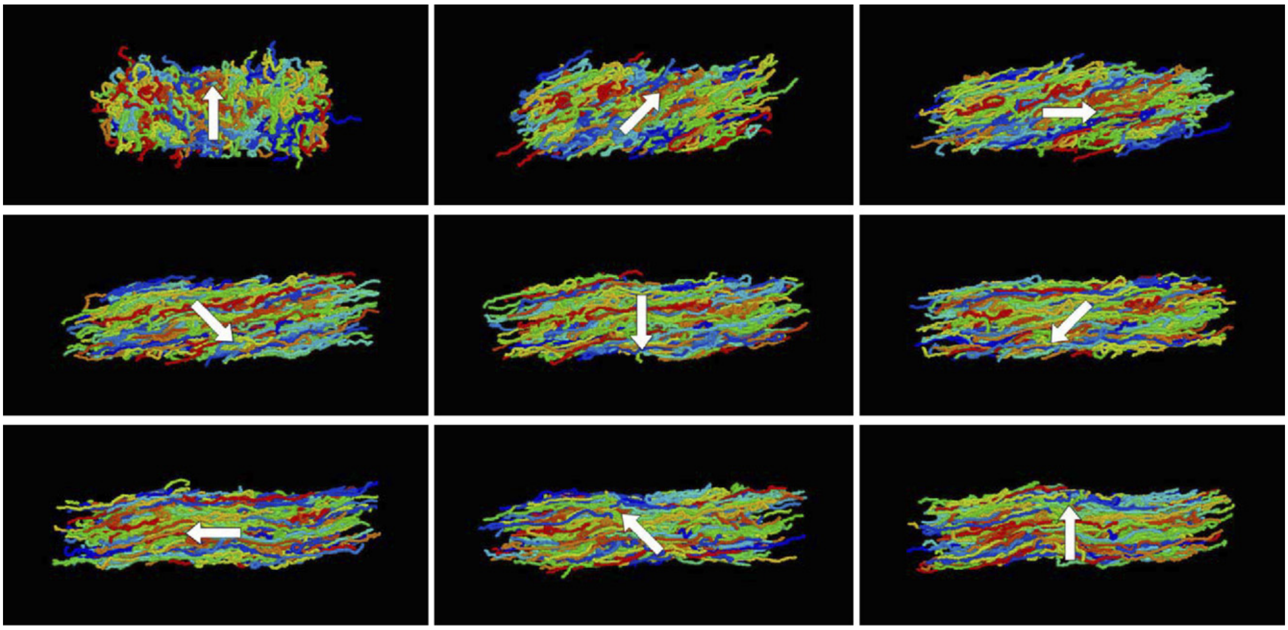

Fig. 10. Snapshots of the $C_{50}H_{102}$ liquid undergoing PCF at a reduced shear rate of 0.8. The shear flow is applied at time zero, and each successive frame is taken at an interval of 4.62 ps. The superimposed arrow indicates the macroscopic rotation of the fluid.

to move axially with greater freedom, which manifests in lower relative stress between the atomistic constituents.

Figs. 10 and 11 present the transient behavior of $C_{50}H_{102}$ under start-up conditions (from equilibrium) of high strain rate PCF and PEF (dimensionless shear rate of 0.8 and elongation rate of 0.2). The arrow is an imaginary visualization of the rotational macroscopic flow field, as quantified by the vorticity vector of the shear field, $\omega = -1/2\nabla \times \mathbf{v}$, where the vector ω quantifies the macroscopic rotation rate. Note that this can be quite different than the rotational rates of the individual atomistic chains. For shear flow, the time interval between each snapshot was 4.62 ps and the total time for one rotation was 36.96 ps. Under PEF, the time interval between each snapshot was 1.616 ps, with the exception of the last one, which was chosen at the starting point of the next application of the KRBC ($t_p = 11.319$ ps). The imaginary box depicts the macroscopic behavior of the simulated liquid. It expands in the flow direction at the rate $x(t) = x\exp(\dot{\varepsilon}t)$, and contracts at the rate of $y(t) = y\exp(-\dot{\varepsilon}t)$, according to the theory of macroscopic fluid dynamics.

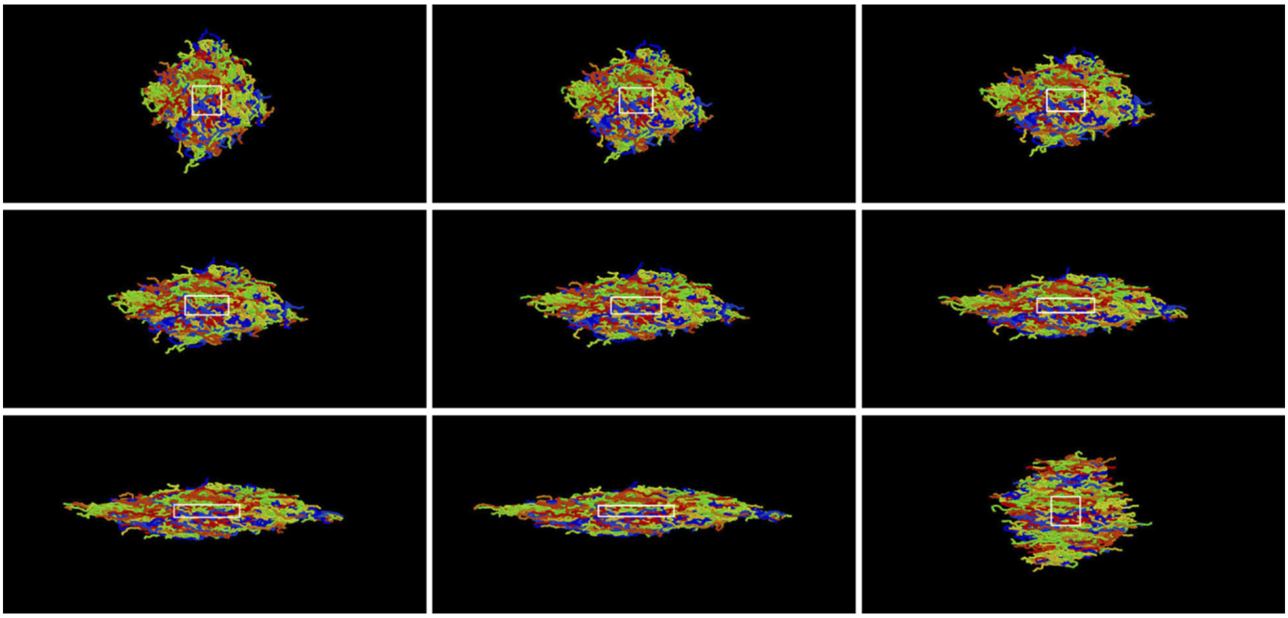

Fig. 11. Snapshots of the $C_{50}H_{102}$ liquid undergoing PEF at a reduced strain rate of 0.2. The elongational flow is applied at time zero, and each successive frame is taken at an interval of 1.616 ps. The superimposed box indicates the macroscopic extension of the fluid.

4. Conclusion

In this work, we visualized and compared the structures of $C_{24}H_{50}$, $C_{50}H_{102}$, $C_{78}H_{158}$, and $C_{128}H_{258}$ at equilibrium, and under PCF and PEF. The snapshots in this paper provide a visual basis for the various statistical measures used to describe polymer orientation and elongation as a function of type of flow, strain rate, and chain length. At equilibrium, the overall shape of each chain adopted a random coil configuration.

Under strong shear flow, a partial alignment and extension of the chains were observed. A dynamical rotation of the chains was also observed due to the vorticity inherent in PCF. These graphics support the statistical description of the molecular configurations as generated from direct measures, such as the conformation tensor, and indirect measures, such as the birefringence. Under strong elongational flow, nearly full alignment of the molecules and extensions approaching the fully *trans*-configuration are observed. The visualization of the primitive paths provided a visual connection between coarse-grained networks and the highly detailed atomistic models. The ability to simulate longer chain molecules likely rests in the ability to perform multiscale simulations that take advantage of both atomistic NEMD simulations and entanglement network dynamics.

Acknowledgments

This research used resources of the Center for Computational Sciences at Oak Ridge National Laboratory, which is supported by the Office of Science of the DOE under Contract DE-AC05-00OR22725. J.M.K. acknowledges support from the Don Bogue fellowship at the University of Tennessee.

References

[1] T. Ionescu, D.J. Keffer, V.G. Mavrantzas, B.J. Edwards, Thermodynamic characterization of polymeric materials subjected to nonisothermal flows: experiment, theory and simulation, J. Rheol., in press.

[2] M. Dressler, B.J. Edwards, H.C. Öttinger, Macroscopic thermodynamics of flowing polymeric liquids., Rheol. Acta 38 (1999) 2028–2043.

[3] A.N. Beris, B.J. Edwards, Thermodynamics of Flowing Systems with Internal Microstructure, Oxford University Press, New York, 1994.

[4] R.B. Bird, O. Hassager, R.C. Armstrong, C.F. Curtiss, 2nd ed., Dynamics of Polymeric Liquids, vol. 2, John Wiley and Sons, New York, 1987.

[5] C. Baig, B.J. Edwards, D.J. Keffer, H.D. Cochran, Rheological and structural studies of liquid decane, hexadecane, and tetracosane under planar elongational flow using nonequilibrium molecular dynamics simulations, J. Chem. Phys. 122 (2005) 184906.

[6] C. Baig, B.J. Edwards, D.J. Keffer, H.D. Cochran, V.A. Harmandaris, Rheological and structural studies of liquid polyethylenes under planar elongational flow using nonequilibrium molecular dynamics simulations, J. Chem. Phys. 124 (2006) 084902.

[7] J.M. Kim, D.J. Keffer, M. Kröger, B.J. Edwards, Rheological and entanglement characteristics of linear chain polyethylene liquids in planar Couette and planar elongational flows, J. Non-Newtonian Fluid Mech., in press.

[8] C. Baig, B. Jiang, B.J. Edwards, D.J. Keffer, H.D. Cochran, A comparison of simple rheological models and simulation data of *n*-hexadecane under shear and elongational flow, J. Rheol. 50 (5) (2006) 625–640.

[9] A.N. Beris, B.J. Edwards, Poisson bracket formulation of incompressible flow equations in continuum mechanics, J. Rheol. 36 (1990) 55–78.

A.N. Beris, B.J. Edwards, Poisson bracket formulation of viscoelastic flow equations of differential type: a unified approach, J. Rheol. 34 (1990) 503–538.

[11] C. Baig, B.J. Edwards, D.J. Keffer, A molecular dynamics study of the stress-optical behavior of a linear short-chain polyethylene melt under shear, Rheol. Acta, in press.

[12] M. Kröger, C. Luap, R. Muller, Polymer melts under uniaxial elongational flow: stress-optical behavior from experiments and nonequilibrium molecular dynamics computer simulations, Macromolecules 20 (1997) 526–539.

[13] M. Kröger, J. Ramirez, H.C. Öttinger, Projection from an atomistic chain contour to its primitive path, Polymer 43 (2002) 477–487.

[14] M. Kröger, Shortest multiple disconnected path for the analysis of entanglements in two- and three-dimensional polymeric systems, Comp. Phys. Commun. 168 (2005) 209–232.

[15] K. Fonteinopoulou, N.C. Karayiannis, V.G. Mavrantzas, M. Kröger, Primitive path identification and entanglement statistics in polymer melts: results from direct topological analysis on atomistic polyethylene models, Macromolecules 39 (2006) 4207–4216.

[16] M. Kröger, Models for Polymeric and Anisotropic Liquids, Springer-Verlag, Berlin, 2005.

[17] C. Tzoumanekas, D.N. Theodorou, Topological analysis of linear polymer melts: a statistical approach, Macromolecules 39 (2006) 4592–4604.

[18] J.D. Schieber, J. Neergaard, S. Gupta, A full-chain, temporary network model with sliplinks, chain-length fluctuations, chain connectivity and chain stretching, J. Rheol. 47 (1) (2003) 213–233.

[19] N.C. Karayiannis, A.E. Giannousaki, V.G. Mavrantzas, D.N. Theodorou, Atomistic Monte Carlo simulation of strictly monodisperse long polyethylene melts through a generalized chain bridging algorithm, J. Chem. Phys. 117 (2002) 5465–5479.

[20] B.J. Edwards, M. Dressler, A reversible problem in non-equilibrium thermodynamics: Hamiltonian evolution equations for non-equilibrium molecular dynamics simulations, J. Non-Newtonian Fluid Mech. 96 (2001) 163–175.

[21] D.J. Evans, G.P. Morriss, Statistical Mechanics of Nonequilibrium Liquids Theoretical Chemistry Monograph Series, Academic Press, London, 1990.

[22] C. Baig, B.J. Edwards, D.J. Keffer, H.D. Cochran, A proper approach for nonequilibrium molecular dynamics simulations of planar elongational flow, J. Chem. Phys. 122 (2005) 114103.

[23] B.J. Edwards, C. Baig, D.J. Keffer, An examination of the validity of nonequilibrium molecular-dynamics simulation algorithms for arbitrary steady-state flows, J. Chem. Phys. 123 (2005) 114106.

[24] B.J. Edwards, C. Baig, D.J. Keffer, A validation of the p-SLLOD equations of motion for homogeneous steady-state flows, J. Chem. Phys. 124 (2006) 194104.

[25] P.J. Daivis, B.J. Todd, A simple, direct derivation and proof of the validity of the SLLOD equations of motion for generalized homogeneous flows, J. Chem. Phys. 124 (2006) 194103.

[26] M. Tuckerman, B.J. Berne, G.J. Martyna, Reversible multiple time scale molecular-dynamics, J. Chem. Phys. 97 (1992) 1990–2001.

[27] J.I. Siepmann, S. Karaborni, B. Smit, Simulating the critical behavior of complex fluids, Nature 365 (1993) 330–332.

[28] W.L. Jorgensen, J.D. Madura, C.J. Swenson, Optimized intermolecular potential functions for liquid hydrocarbons, J. Am. Chem. Soc. 106 (1984) 6638–6646.

[29] A.M. Kraynik, D.A. Reinelt, Extensional motions of spatially periodic lattices, Int. J. Multiphase Flow 18 (1992) 1045–1059.

[30] L.R.G. Treloar, The Physics of Rubber Elasticity, Oxford University Press, Oxford, 1975.

[31] M. Doi, S.F. Edwards, The Theory of Polymer Dynamics, Oxford University Press, Oxford, 1986.

[32] G.P. Morriss, P.J. Daivis, D.J. Evans, The rheology of *n*-alkanes: decane and eicosane, J. Chem. Phys. 94 (1991) 7420–7433.

[33] S.T. Cui, S.A. Gupta, P.T. Cummings, H.D. Cochran, Molecular dynamics simulations of the rheology of normal decane, hexadecane, and tetracosane, J. Chem. Phys. Rev. 105 (1996) 1214–1220.

[34] J.D. Moore, S.T. Cui, H.D. Cochran, P.T. Cummings, A molecular dynamics study of a short-chain polyethylene melt. I. Steady-state shear, J. Non-Newtonian Fluid Mech. 93 (2000) 83–99.